Monthly Notices of the ROYAL ASTRONOMICAL SOCIETY

MNRAS **548,** 1–17 (2026)
Advance Access publication 2026 April 14

https://doi.org/10.1093/mnras/stag688

Reconciling near-infrared and microwave analyses of Neptune's hydrogen sulphide distribution

Joseph Penn [1]★ Patrick G. J. Irwin [1] Jack Dobinson,[1] Leigh N. Fletcher,[2] Nicholas A. Teanby[3] and Michael T. Roman[2,4]

[1]*Atmospheric, Oceanic and Planetary Physics, Department of Physics, University of Oxford, Parks Road, Oxford, UK*
[2]*School of Physics and Astronomy, University of Leicester, University Road, Leicester, UK*
[3]*School of Earth Sciences, University of Bristol, Queens Road, Bristol, UK*
[4]*Facultad de Ingeniería y Ciencias, Universidad Adolfo Ibáñez, Av. Diagonal Las Torres 2640, Santiago, Chile*

Accepted 2026 April 7. Received 2026 March 30; in original form 2026 February 4

ABSTRACT

Previous analysis of Neptune's atmosphere using near-infrared Gemini/NIFS observations found the strongest spectral signature of hydrogen sulphide (H_2S) to be at the planet's south pole. Conversely, analysis of microwave observations with the Atacama Large Millimeter/submillimeter Array in 2019 suggested a distribution of H_2S that peaks in the mid-latitudes and is strongly depleted towards the pole. We analyse near-infrared observations from VLT-SINFONI in 2018 and fit a parametrized cloud model to the data using nested sampling. By prescribing a latitudinally varying methane (CH_4) profile previously derived from visible light observations, we find general agreement with the microwave analysis, with an enhancement of H_2S by a factor of ∼4 at the southern mid-latitudes compared to polar latitudes. The stronger spectral signature at the pole is explained with a deeper cloud top, resulting in a higher cloud-top H_2S column abundance in this region. Our results are indicative of deep upwelling at the mid-latitudes, with downwelling at the pole and possibly near the equator.

Key words: radiative transfer – scattering – techniques: imaging spectroscopy – planets and satellites: atmospheres.

1 INTRODUCTION

Hydrogen sulphide (H_2S) is expected to be the primary constituent of Neptune's 5–7 bar cloud deck (P. G. J. Irwin et al. 2022), and determining how the H_2S abundance varies with latitude is important for understanding the planetary circulation. In Neptune's cold troposphere, temperatures are low enough for most gases to condense below the 10-bar pressure level; at lower pressures the primary constituents are expected to be H_2, He, CH_4, N_2, and H_2S. Alongside the H_2S cloud, a second major cloud deck is expected from CH_4 condensation around 1–2 bar (P. G. J. Irwin et al. 2022).

Horizontal variations of CH_4 can provide insight into the planetary circulation (L. N. Fletcher et al. 2020). Analysis of visible and near-infrared reflectance spectra has revealed that the CH_4 mole fraction at pressures deeper than its condensation level is about twice as high at equatorial latitudes as it is at the poles (E. Karkoschka & M. G. Tomasko 2011; P. G. J. Irwin et al. 2023). This has typically been interpreted as a sign of upwelling here – deep, CH_4-rich air rises near the equator and produces the increased abundance. This air moves polewards along a circulation cell, drying out as the CH_4 condenses, and then descends nearer the pole, causing a depleted abundance of the gas there. In this way, by determining the CH_4 variation with latitude, it is possible to gain an understanding of the overturning circulation near the CH_4 condensation level.

How does this circulation vary with depth? One way to answer this question is to compare variations of H_2S with CH_4. Most of the H_2S in the Ice Giants is expected to react with NH_3 and form a deep cloud of solid NH_4SH at ∼40 bar (S. K. Atreya & A.-S. Wong 2005), but, if there is more H_2S than NH_3, the remaining unreacted H_2S is free to condense at lower pressures. Because H_2S condenses deeper in the atmosphere than CH_4, it allows us to probe the deeper circulation. However, analyses using microwave (J. Tollefson et al. 2019) and near-infrared (P. G. Irwin et al. 2019) observations have shown very different H_2S distributions. It is crucial to determine why these results are so different so that we can properly understand Neptune's H_2S distribution and thus its circulation patterns.

J. Tollefson et al. (2019) used spatially resolved millimetre-wave observations with the Atacama Large Millimeter/submillimeter Array (ALMA) to determine the latitudinal distributions of CH_4 and H_2S by analysing the variation of Neptune's brightness temperature. The best fits to their observations gave them subsaturated H_2S profiles at polar latitudes and supersaturated H_2S near the equator. They also found an increase in the deep CH_4 abundance from the pole to mid-latitudes.

★ E-mail: joseph.penn@physics.ox.ac.uk

Table 1. VLT/SINFONI observation details. Integration times for the low angular resolution observations were 60s, and integration times for each mosaic tile were 70s.

ID	Date	Time (UT)	Airmass	Pixel size (arcsec)	Mosaic tiles
1	18 Aug 2018	04:19:09	1.163	0.1	1
2	19 Aug 2018	09:54:39	1.949	0.1	1
3	31 Aug 2018	05:31:21	1.055	0.1	1
4	31 Aug 2018	06:01:51	1.076	0.1	1
5	19 Sept 2018	03:10:44	1.066	0.025	16
6	26 Sept 2018	04:49:35	1.122	0.025	16
7	27 Sept 2018	03:58:01	1.063	0.025	17
8	27 Sept 2018	05:14:33	1.186	0.025	17
9	27 Sept 2018	06:31:14	1.522	0.025	17
10	28 Sept 2018	03:45:52	1.057	0.025	17
11	30 Sept 2018	01:57:37	1.098	0.025	17

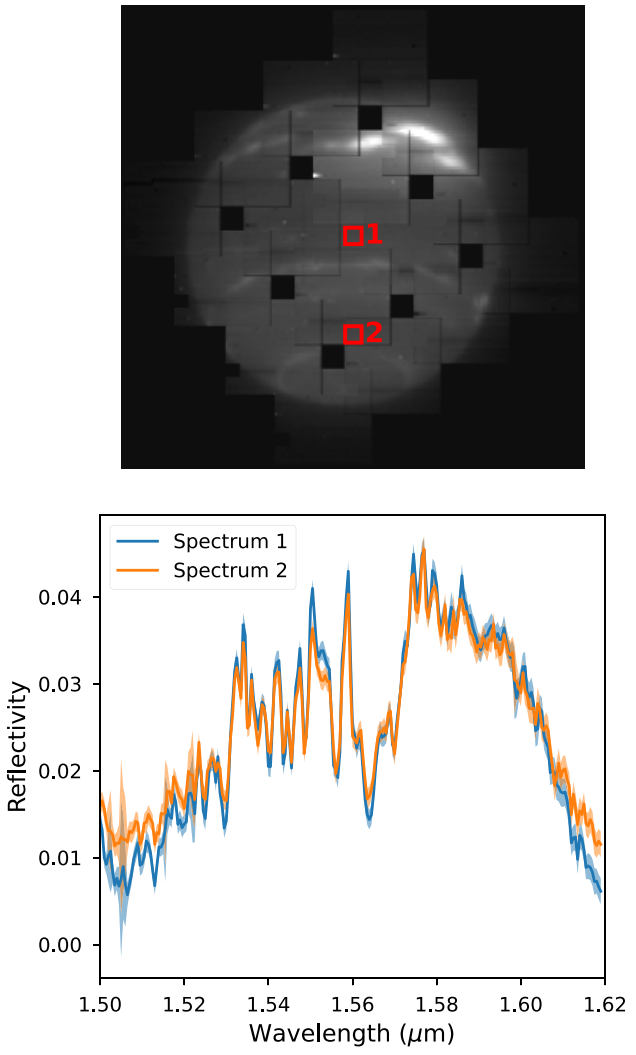

Figure 1. Top: Cube 5 averaged over 1.50–1.62 μm, our wavelength range of interest. Two numbered boxes are shown, and the average spectra in these boxes are shown in the lower figure with error estimates (shaded region).

Conversely, P. G. Irwin et al. (2019) used observations from Gemini/NIFS to detect the spectral signature of H_2S in a small wavelength range around 1.58 μm, finding a much stronger signature at the pole than near the equator. They found a higher column abundance of the gas above the clouds at polar regions, and concluded that there is a higher volume mixing ratio (VMR) of H_2S here. This conflicts with the conclusion of J. Tollefson et al. (2019), who argued that the H_2S VMR is lowest at the pole. The latitudinal distribution of H_2S found from the microwave analysis is somewhat similar to the distribution of CH_4 – this would suggest that the tropospheric pattern of upwelling at equatorial latitudes and downwelling at polar latitudes extends deep into the atmosphere. On the other hand, the findings from the near-infrared analysis could indicate upwelling at the pole at the H_2S condensation level – and thus a significant change in the circulation with depth. These analyses are difficult to reconcile, as they use different wavelength ranges (microwave thermal emission versus near-infrared reflection) that are sensitive to different altitudes (with ALMA sounding much deeper than NIFS).

In this work, we aim to resolve the apparent discrepancy between these results by analysing centre-to-limb variations of high-resolution near-infrared spectra of Neptune. We show that the assumed CH_4 abundance strongly affects the retrieved H_2S distribution, so we account for this in our modelling.

2 DATA

Observations were made in 2018 using the Spectrograph for INtegral Field Observations in the Near Infrared (SINFONI; F. Eisenhauer et al. 2003) on the European Southern Observatory's Very Large Telescope (Table 1). SINFONI was an integral field spectrograph, producing spectral cubes of 64x64 spectra with 2048 wavelengths. Some of the observations were made using SINFONI's smallest pixel scale (0.025 arcsec) in its H + K band mode, with a resolving power of $\lambda/\Delta\lambda \approx 1500$ over a wavelength range of 1.45–2.45 μm. When using this pixel scale, the field of view is 0.8 arcsec x 0.8 arcsec, which is significantly smaller than the angular diameter of Neptune ($\sim$ 2.3 arcsec). To capture the whole disc, a mosaic of the planet must be constructed using the smaller exposures. Taking observations in the high spatial resolution mode reduces the spread of scattered light from bright, discrete upper tropospheric clouds, giving a clearer view of the underlying atmosphere. Seven mosaics were produced. Some of the edges of the mosaic tiles (i.e. the edges of the instrument's field of view) are dimmer than the rest of the tile due to vignetting effects. We manually masked out these pixels so that they would not be considered in our analysis. Some of the mosaics are also missing regions of the disc - naturally we masked out these regions as well. Four observations using a larger pixel scale (0.1 arcsec) were also taken in 2018. Neptune fits into the field of view of these observations so no mosaicking was required. For all the observations, the SINFONI adaptive optics system was used to improve the image quality.

A significant portion of the spectrum lies below the noise floor of the instrument, so is not usable. However, the 1.50–1.62 μm window, within which the H_2S signature lies, is significantly brighter than the rest of the spectrum and is suitable for analysis. An example cube and spectrum are shown in Fig. 1, and all the cubes are shown in Fig. 2. Error estimates were derived from the standard deviation of pixel values where the instrument was viewing empty space. The per-pixel errors were found to typically be $\sim$10 per cent of the average reflectivity at a given wavelength.

In Section 3.2.1, we incorporate the limb-darkening behaviour of Neptune's atmosphere into our analysis. Because we assume a zonally symmetric atmosphere, we must mask out the dis-

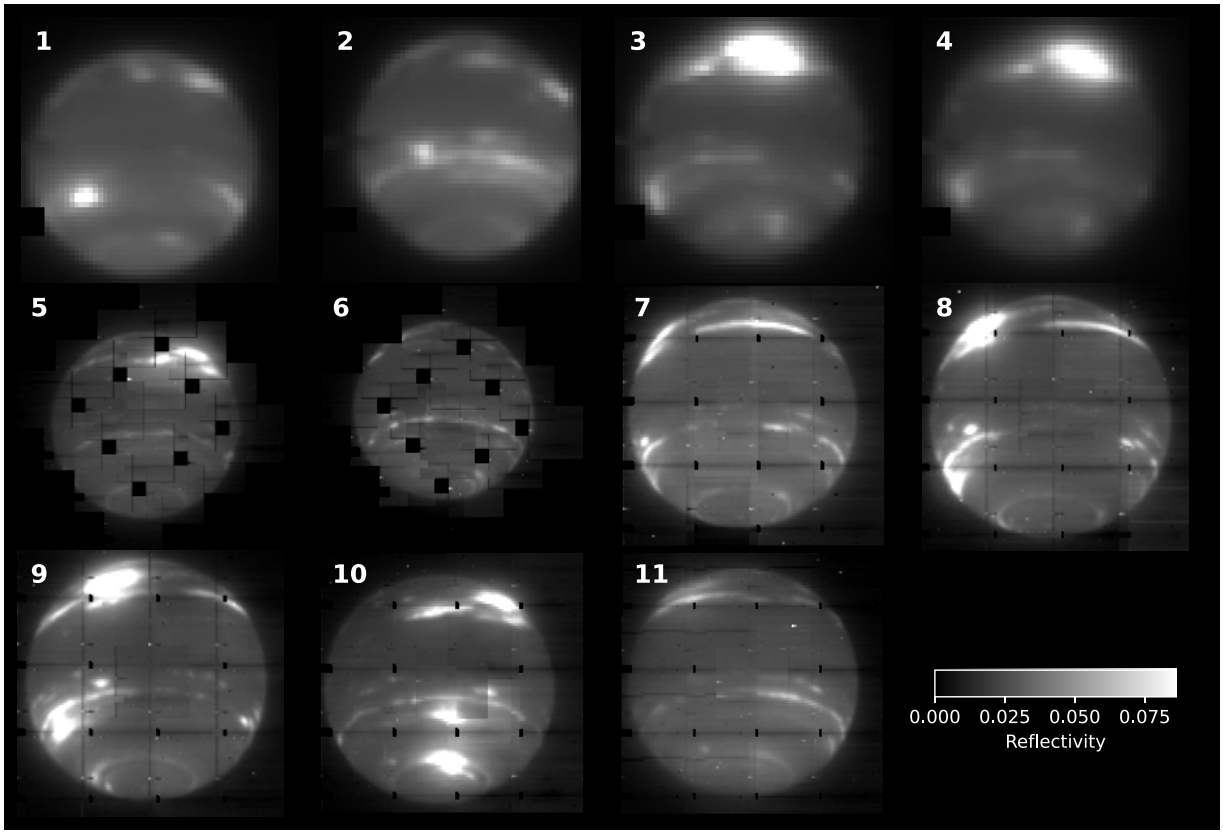

Figure 2. The 11 observations analysed in this study. Numbers at the top left of each observation correspond to Table 1. Many cloud bands and larger discrete clouds can be observed, along with several artefacts from the mosaicking process. The observations have been averaged over 1.50–1.62 μm.

crete clouds that are present in our observations. To determine a suitable threshold for masking out clouds, we inspected the histogram of reflectivity of all our cubes, averaged across the 1.50–1.62 μm region. We found that a threshold on the averaged reflectivity of 0.03 was suitable for masking out the clouds without the bulk of the disc being affected. We then used a binary dilation operation on this mask to capture any edges of the clouds that the threshold might have missed.

3 RADIATIVE TRANSFER ANALYSIS

We initially used spectral line data from HITRAN 2020 (I. Gordon et al. 2022) for both CH_4 and H_2S. However, similar to P. G. Irwin et al. (2019), we later found that using CH_4 line data from the 'WKLMC@80K + ' data base (A. Campargue et al. 2013) significantly improved our goodness of fit – this line data was also used by P. G. Irwin et al. (2019). We converted this data into line-by-line lookup tables at a range of pressures and temperatures which follow the Neptunian P-T profile. Typically, when computing the opacity of a gas in a certain wavelength bin, the correlated-k method (A. A. Lacis & V. Oinas 1991) is used. The spectral distribution of opacity within each wavelength bin can be represented by a relatively small number (10–20) of quadrature points, facilitating the efficient calculation of mean opacities. Assuming that the k-distributions of different paths within an inhomogeneous atmosphere are spectrally correlated, transmissions can be multiplied together, which is important for multiple scattering calculations. In this work, we instead use a line-by-line method, where the spectrum is computed at a very high spectral resolution before being convolved with the instrument function. This relies on fewer assumptions than the correlated-k method and so is more accurate, but is more computationally costly. For the CH_4 line data, we used the recommendation of J.-M. Hartmann et al. (2002) – a sub-Lorentzian lineshape for CH_4 in a hydrogen atmosphere. For the line shape of H_2S we used a simple Voigt function. For both gases we used a large line wing cut-off of 100cm^{-1} (∼25nm at 1.6 μm). We found it was necessary to compute our spectrum at a very fine resolution (0.04nm) before convolving with the instrument function in order to closely match our measurements. For the instrument function, we used a Gaussian with a FWHM of 1 nm – corresponding to a resolving power of 1500 at 1.5 μm, as expected from SINFONI in its H + K mode.

For our solar spectrum, we used the spectrum of M. Meftah et al. (2023). Again, we found that a high spectral resolution of 0.04nm was necessary to match the measured spectrum - retrievals using lower resolution solar spectra did not achieve the same goodness of fit.

The reference temperature and mole fraction profiles are those used by P. G. J. Irwin et al. (2022) and are based on the 'N' profile determined from radio occultation measurements by Voyager 2 (G. F. Lindal 1992). We assume a constant temperature profile with latitude and a H_2:He ratio of 85:15. Although CH_4 is the dominant absorber in our wavelength range, we do include the effects of H_2–H_2 and H_2–He collision induced absorption. We assume that the ortho:para hydrogen ratio is in thermal equilibrium and we use absorption data from A. Borysow & L. Frommhold (1989). We assume a simple CH_4 model with a constant deep

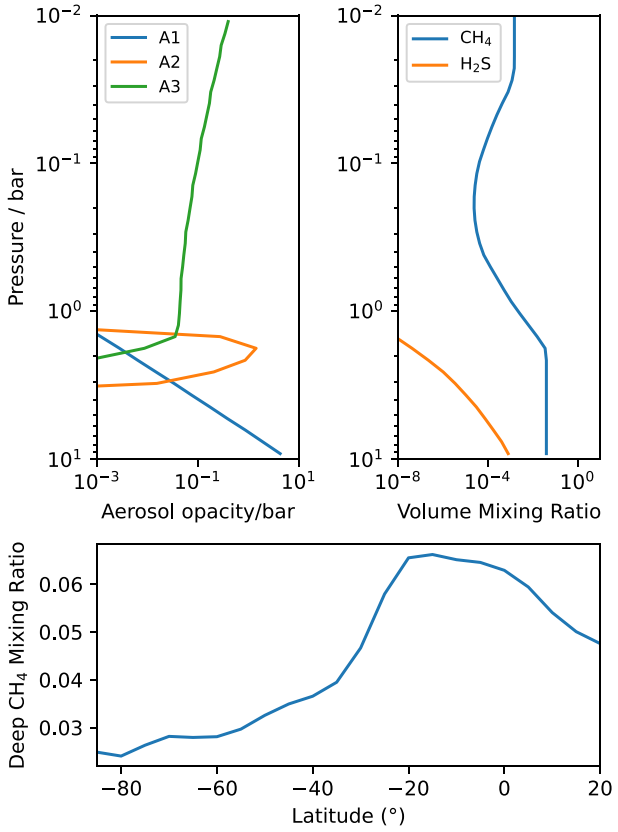

Figure 3. Base profiles used in retrievals. Top left: Aerosol opacity for the three layers against pressure. Top right: VMR for the two radiatively active gases in the model. Bottom: Deep CH_4 VMR with latitude from P. G. J. Irwin et al. (2023).

VMR, a fixed relative humidity above the condensation level of 50 per cent and a fixed stratospheric VMR of $1.5\text{x}10^{-3}$ (Lellouch et al. 2010). We use a $^{13}CH_4/CH_4$ fraction of 1 per cent and a CH_3D/CH_4 fraction of 0.03 per cent, in keeping with the results from P. Irwin et al. (2014). Our reference H_2S profile has a deep VMR of 10^{-3}, and follows the saturation vapour pressure curve as the temperature decreases with increasing height (Fig. 3). In our retrievals we apply a simple multiplicative scaling factor to this profile and allow arbitrarily high supersaturations. Because the spectral signature is so subtle, we are not sensitive enough to determine vertical variations of H_2S, and so this simple scaling factor is sufficient for our study.

P. G. J. Irwin et al. (2023) used a limb-darkening approximation and a 'holistic' parametrized cloud model to determine the variation of aerosol opacity, aerosol scattering properties, and deep CH_4 abundance across a large latitude range from observations using VLT's MUSE instrument. We fixed the deep CH_4 abundance in our model to this latitudinally varying profile (Fig. 3).

3.1 Simplified Band-Depth Modelling

To better understand our data and any potential degeneracies, we first performed some preliminary simple modelling. The H_2S spectral signature is strongest in the 1.58–1.60 μm region (Fig. 4), where absorption from CH_4 is relatively weak. In this region, we can attempt to approximate the reflectivity of the atmosphere with a band-depth approximation, similar to P. G. J. Irwin et al. (2025). We write the reflectivity, (I/F), as

$$(I/F) = (R_0 + R_1\lambda)e^{-x_{\mathrm{CH_4}}k_{\mathrm{CH_4}}(\lambda) - x_{\mathrm{H_2S}}k_{\mathrm{H_2S}}(\lambda)}, \quad (1)$$

where $R_0 + R_1\lambda$ is a linear function of wavelength to fit the continuum, x_{CH_4} and x_{H_2S} are the cloud-top column abundances of CH_4 and H_2S, and $k_{CH_4}(\lambda)$ and $k_{H_2S}(\lambda)$ are their absorption coefficients.

We assume that there is a reflecting cloud top at some pressure level in the atmosphere. There is an inherent degeneracy between the CH_4 distribution and the retrieved H_2S abundance, as we must use the CH_4 abundance to determine the cloud-top pressure, which we then use to infer the H_2S scaling factor (Fig. 5). However, because we are assuming a known latitudinal distribution of CH_4, and a known dependence of H_2S abundance with pressure (Fig. 3), we are able to use our fitted column abundances to determine the H_2S scaling factor everywhere on the disc.

We write our CH_4 and H_2S abundances per bar as a function of pressure ($f_{CH_4}(p)$ and $f_{H_2S}(p)$, respectively). Then, our cloud-top column abundance of CH_4 is the integral of $\eta f_{\mathrm{CH_4}}(p)$ from the top of the atmosphere to our cloud-top pressure, where η is an airmass factor (2 for nadir-viewing):

$$x_{\mathrm{CH_4}} = \eta \int_0^{p_{top}} f_{\mathrm{CH_4}}(p)\,\mathrm{d}p = \eta F_{\mathrm{CH_4}}(p_{\mathrm{top}}), \quad (2)$$

where $\frac{\mathrm{d}F}{\mathrm{d}p} = f$. We can solve for the cloud-top pressure in terms of F^{-1}, the inverse of F:

$$p_{\mathrm{top}} = F^{-1}_{\mathrm{CH_4}}\left(\frac{x_{\mathrm{CH_4}}}{\eta}\right). \quad (3)$$

Our H_2S cloud-top column abundance has an identical form as for CH_4, but with the additional multiplication of our scaling factor, S, which is applied to the H_2S profile:

$$x_{\mathrm{H_2S}} = S\eta \int_0^{p_{\mathrm{top}}} f_{\mathrm{H_2S}}(p)\,\mathrm{d}p. \quad (4)$$

We now integrate and rearrange for S:

$$S = \frac{x_{\mathrm{H_2S}}}{\eta F_{\mathrm{H_2S}}(p_{\mathrm{top}})}. \quad (5)$$

Substituting in our expression for p_{top}, we can find an expression for S in terms of our airmass factor and the two cloud-top column abundances:

$$S = \frac{x_{\mathrm{H_2S}}}{\eta F_{\mathrm{H_2S}}\left(F^{-1}_{\mathrm{CH_4}}\left(\frac{x_{\mathrm{CH_4}}}{\eta}\right)\right)}. \quad (6)$$

We found that the high spatial resolution cubes were too noisy to do this on a pixel-by-pixel scale. Hence, we averaged them into 4x4 pixel bins (side length 0.1arcsec). We performed our band-depth analysis on these averaged cubes and the lower spatial resolution cubes to retrieve the cloud-top pressure and H_2S scaling factor. An example of the analysis on one of the lower resolution cubes is shown in Fig. 6. The results, averaged into latitude bins, are shown in Fig. 7. Our retrieved H_2S scaling factor is highly sensitive to the cloud-top pressure and hence to the CH_4 abundance. In agreement with P. G. Irwin et al. (2019), we find a higher cloud-top column abundance of H_2S at the pole (and thus a stronger spectral signature); however, we find peaks of the deep abundance of H_2S at 20°S and north of the equator (Fig. 7). The reason for this difference is that the cloud-top pressure is significantly lower near the equator than near the pole.

To confirm that we are really seeing H_2S, we can attempt to isolate the spectral signature. If we take the ratio of two reflectiv-

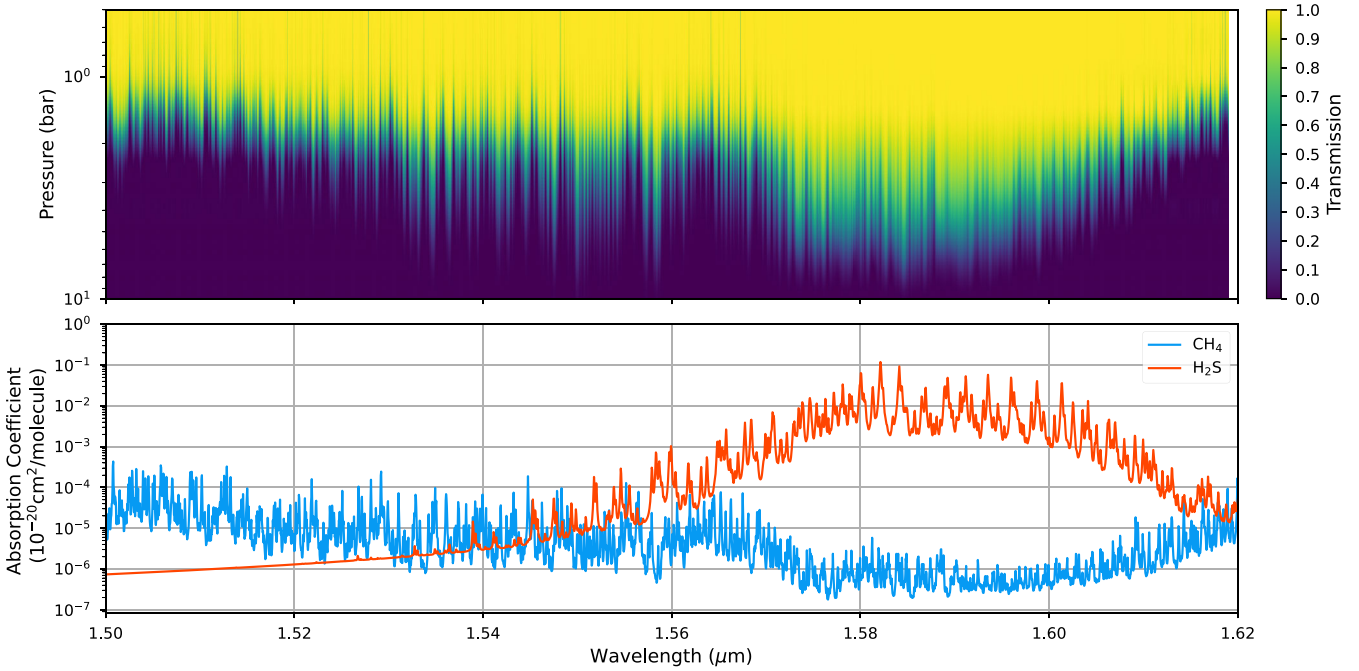

Figure 4. Top: Two-way transmission from space for a vertical path to different pressures in our model atmosphere (shown in Fig. 3), assuming no aerosols. In reality, there is a cloud top expected at 2–4 bar which causes strong scattering, so we are unlikely to be sounding as deeply as 10 bar. Bottom: Absorption spectra of CH_4 and H_2S at 1 bar and 70 K. Although the H_2S absorption is much stronger than CH_4 at many wavelengths, its abundance is much lower and so it is still challenging to detect.

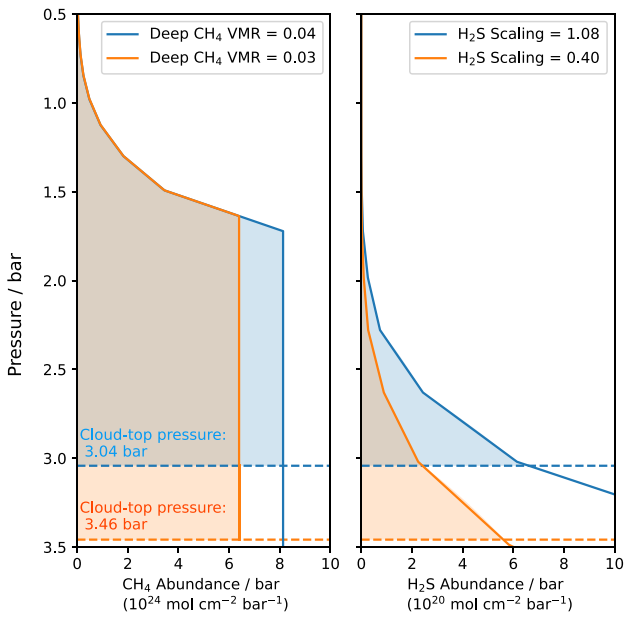

Figure 5. Demonstration of the degeneracy between CH_4 and H_2S. If we prescribe a lower deep CH_4 abundance, we must set our cloud top to be deeper in the atmosphere in order to have the correct CH_4 cloud-top column abundance. The deeper cloud top means that we must reduce our H_2S scaling factor to have the correct H_2S cloud-top column abundance.

ities from two locations on the planet (with subscripts 0 and 1), we obtain

$$\frac{(I/F)_0}{(I/F)_1} = \frac{R_{0,0} + R_{1,0}\lambda}{R_{0,1} + R_{1,1}\lambda} e^{\Delta x_{\mathrm{CH_4}} k_{\mathrm{CH_4}}(\lambda) + \Delta x_{\mathrm{H_2S}} k_{\mathrm{H_2S}}(\lambda)}, \quad (7)$$

where $\Delta x_{CH_4} = x_{CH_4,1} - x_{CH_4,0}$ and the same for Δx_{H_2S}. We can then take the natural logarithm of this equation:

$$\log\left(\frac{(I/F)_0}{(I/F)_1}\right) = \log\left(\frac{R_{0,0} + R_{1,0}\lambda}{R_{0,1} + R_{1,1}\lambda}\right) + \Delta x_{\mathrm{CH_4}} k_{\mathrm{CH_4}}(\lambda) + \Delta x_{\mathrm{H_2S}} k_{\mathrm{H_2S}}(\lambda). \quad (8)$$

Our band-depth analysis has shown that the cloud-top column abundance of CH_4 is fairly uniform across the disc, but the cloud-top column abundance of H_2S is enhanced at the pole. We average the reflectivity spectra from the south polar region (60°S to 90°S) and the equatorial region (5°S to 5°N). Plotting the logarithm of the ratio of averaged reflectivities over the 1.58–1.60 µm range, the H_2S spectral signature is clearly visible (Fig. 8). This is where the H_2S absorption features are strongest compared to CH_4 (Fig. 4), and since we are only looking in this small wavelength range we can assume for simplicity that the first term on the right hand side of equation (8) is a constant (i.e. the two regions have similar continuum spectral slopes). We fit $\Delta x_{\mathrm{CH_4}}$, $\Delta x_{\mathrm{H_2S}}$, and this constant to the logarithm of the ratio. We find that the effect of differences in the cloud-top CH_4 column abundance are negligible here, and the undulations show agreement with the H_2S spectrum. This is strong evidence that we are indeed able to detect H_2S above Neptune's clouds.

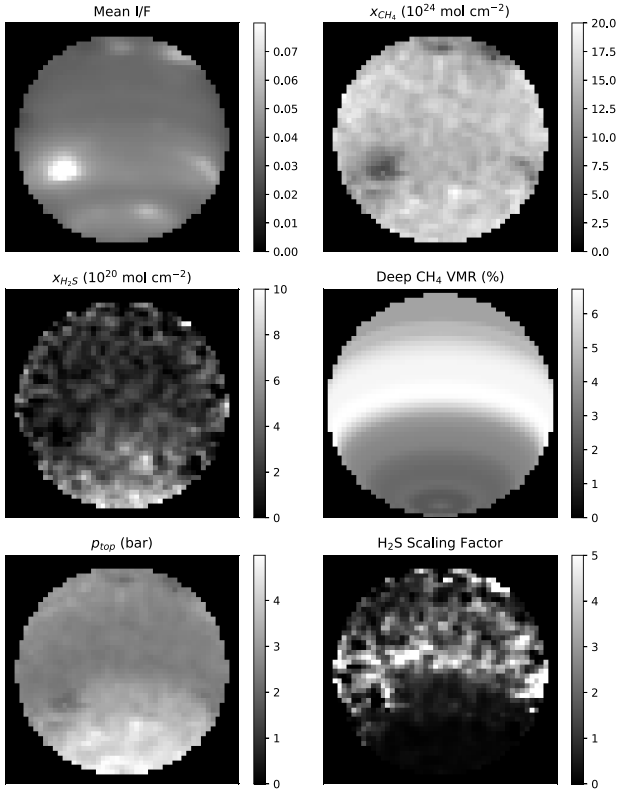

Figure 6. Top left: Mean reflectivity over all wavelengths from 1.58–1.60 μm in Observation 1. Top right: Retrieved cloud-top column abundance of CH_4. Middle left: Retrieved cloud-top column abundance of H_2S, showing an increase at the south pole. Middle right: Prescribed variation of CH_4 with latitude from P. G. J. Irwin et al. (2023). Bottom left: Derived cloud-top pressure, showing a deeper cloud at the south pole. Bottom right: Derived H_2S scaling factor, showing a strong depletion at the pole and enhancement at the mid-latitudes.

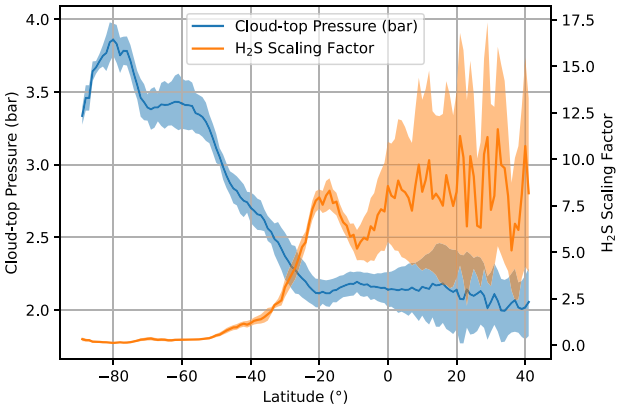

Figure 7. Retrieved H_2S scaling factor and cloud-top pressure with latitude, averaged over all 4 low angular resolution observations. The values have been rebinned into bins of width 2° and spacing 1°. North of the equator, the results are very noisy due to the lack of pixels and significant presence of discrete clouds. Shading indicates the standard deviation of the parameters in each latitude bin.

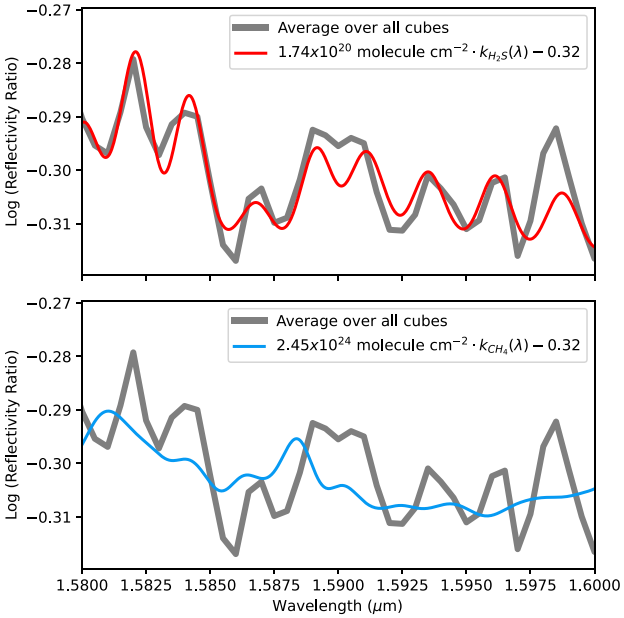

Figure 8. Top: Natural log of the equatorial/polar reflectivity ratio. It can be seen that the fitted H_2S absorption spectrum (red) can explain the undulations. Bottom: The same, with a fitted CH_4 absorption spectrum instead. This is a much poorer fit. Absorption spectra are at 2 bar and 90 K, and have been smoothed to the spectral resolution of SINFONI.

3.2 Retrievals

This simple band-depth analysis technique already gives us an improved idea of the true H_2S variation. We seek to verify the results with a more robust approach, by using a realistic aerosol structure, fitting to a larger region of the spectrum (1.5–1.62 μm), and employing a retrieval scheme that uses multiple scattering to determine the reflected radiance of the atmosphere.

3.2.1 Minnaert limb-darkening fitting

To average our observations into latitude bands, we use the Minnaert limb-darkening approximation (M. Minnaert 1941), which has been successfully applied in several previous studies of the Ice Giants (e.g. P. G. J. Irwin et al. (2022, 2023), A. James et al. (2023)). This approximation allows us to write the reflectivity of the atmosphere, I/F, in terms of the reflectivity at the nadir $(I/F)_0$, a limb-darkening coefficient k, and the cosines of the viewing and solar zenith angles (μ and μ_0 respectively):

$$(I/F) = (I/F)_0 \mu_0^k \mu^{k-1} \approx (I/F)_0 \mu_0^{2k-1}. \quad (9)$$

For observations of Neptune from Earth, $\mu \approx \mu_0$ as we are relatively very close to the Sun. At each wavelength, we can fit $(I/F)_0$ and k to the observed radiance across the disc, or across a selected latitude band. We can then use these fitted parameters to reproduce spectra at any zenith angle. This allows us to average over all spectra in a region, reducing noise, and means we are also able to fit our model to the limb-darkening behaviour of the atmosphere, which helps to differentiate between gas and aerosol opacity.

As discussed in Section 2, we masked out bright discrete clouds to avoid unwanted effects on our limb-darkening analysis. The observations were split into latitude bands with width 10° and

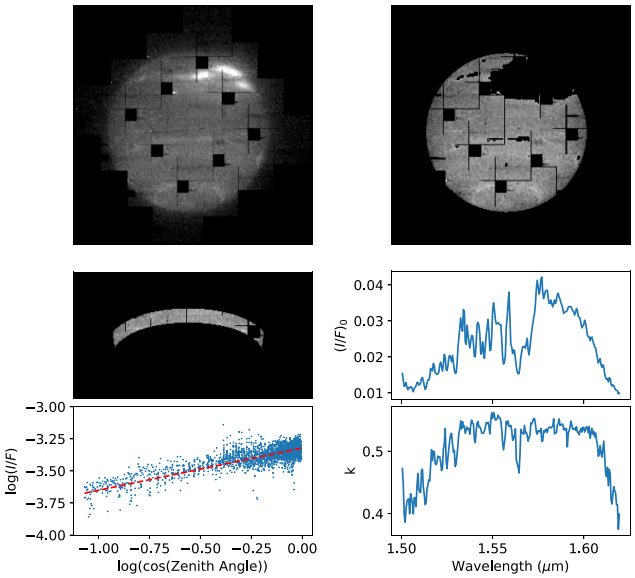

Figure 9. Demonstration of the steps in our Minnaert fitting pipeline applied to Observation 5. The raw mosaic (top left) has clouds, background, and hot pixels masked out to produce the top right image. Then, a latitude band is selected (middle left, 20°S to 10°S) and at each wavelength the Minnaert parameters are fitted (bottom left, 1.58 μm shown). This produces spectra of nadir reflectivity (middle right) and limb-darkening coefficient (bottom right).

spacing 5° to achieve Nyquist sampling. The Minnaert approximation was then applied to each latitude band in each observation mosaic (Fig. 9). The fitted parameters, shown in Figs 10 and 11, were used to generate spectra at viewing angles of 0.0° and 61.45°. These fitted spectra were then averaged over all the observations to obtain average spectra at each latitude band. These angles were chosen as they correspond to two of the angles in our multiple scattering quadrature scheme; the radiance is explicitly calculated at these angles and so we avoid errors from interpolation. This approach has been used in previous studies, e.g. P. G. J. Irwin et al. (2022).

Each pixel spectrum in our observations has an uncertainty of around 10 per cent of the peak radiance. However, the Minnaert approximation allows us to average over several thousand pixels for each latitude band. Because of this, the errors on our reconstructed spectra are very small. Even for the 80°S to 90°S latitude band, we have ∼2500 pixels across our seven cubes. Despite the restricted range of zenith angles in this latitude band (55°to 74°), simple least-squares fitting still gives small uncertainties (roughly 1 per cent) on our Minnaert parameters here. Where we have more coverage of a latitude band, this error will be even smaller (e.g. ∼ 0.07 per cent between 20°S and 30°S). Unfortunately, we were unable to fit our radiative transfer models to this level of accuracy. Similar to P. G. J. Irwin et al. (2023) and A. James et al. (2023), we found that we were able to fit the disc-averaged Minnaert-reconstructed spectra to $\chi^2_\nu \approx 1$ if we assumed the error at all wavelengths to be equivalent to 2 per cent of the peak radiance. This error encompasses systematic errors in the data, deficiencies in our forward modelling and limb-darkening approximation, inhomogeneities in the atmospheric structure, and uncertainties on the CH_4 and H_2S absorption coefficients. Here, χ^2_ν refers to the χ^2 statistic divided by the total degrees of freedom, which is the number of wavelengths minus the number of free parameters.

3.2.2 *Aerosol model*

To model the near-infrared/visible reflected sunlight spectra of Uranus and Neptune, P. G. J. Irwin et al. (2022) proposed a 'holistic' aerosol model, consisting of three/four aerosol layers for Uranus and Neptune respectively – this model was found to fit the spectra of these planets to a high degree of accuracy over a large wavelength range. The deepest aerosol layer, at ∼5–7 bar, is theorized to be composed of photochemical haze along with H_2S ice. In the original holistic model, this layer was modelled as vertically extended, with its opacity increasing with depth, but the model has since been updated (P. G. J. Irwin et al. 2023) with a vertically thin cloud instead. The second layer is at around 2 bar, and is composed of CH_4 ice along with photochemical haze. The third layer comprises photochemical haze and extends upwards to the stratosphere where this haze is likely to be produced. The fourth layer is used for modelling bright, upper tropospheric clouds (assumed to be composed of CH_4 ice) in Neptune's atmosphere when necessary.

We use a parametrized aerosol model, similar to that of P. G. J. Irwin et al. (2022), with three aerosol layers. Initially, we prescribed discrete, highly scattering layers at 5 bar and 2 bar and an extended haze layer from 1.6 bar to the stratosphere. The data show a very flat limb-darkening curve (Fig. 11) with k close to 0.5 (no limb darkening or brightening) at most wavelengths, which this aerosol model struggled to replicate. In order to achieve a χ^2_ν value of approximately 1, we found it was necessary to let the imaginary refractive indices (absorption coefficients) of the 2 bar aerosol layer and the extended haze layer vary with wavelength. However, for the deepest layer, n_{imag} was fixed to 10^{-4} (highly scattering) at all wavelengths. We also found that fits were significantly improved by replacing the deepest layer at 5 bar with an extended layer with its base at 10 bar (the deepest pressure level in our model). The fractional scale height of the layer was allowed to vary. Although we are not actually able to sound very deeply into this layer, this change allowed us to more easily vary the height of the deep cloud top. Note that this is more similar to the original holistic model for the Ice Giants (P. G. J. Irwin et al. 2022) - the model was later updated in P. G. J. Irwin et al. (2023) to use a discrete layer here to aid in retrieval stability.

Of course, just because a model provides a single better fit to the data (and thus achieves a lower χ^2_ν), this does not necessarily mean it is a better model. Ideally, we would use a Bayesian optimization method such as nested sampling to compute the Bayesian evidence for all of our model experiments, and compare models based on this. However, we found that computing the Bayesian evidence for all of our model choices would be prohibitively slow. Throughout our initial exploratory analysis, we used the χ^2_ν value of the best-fitting spectrum (determined with optimal estimation) as a simple diagnostic to see which changes would make a significant difference.

We assumed standard gamma size distributions for our aerosol particles, with size parameters given in Table 2.

These were based on the analysis from P. G. J. Irwin et al. (2023). We experimented with adjusting the size distributions but found no improvements in the goodness of fit – it is likely that the imaginary refractive index spectrum can adjust to accommodate a large range of prescribed size distributions over our relatively

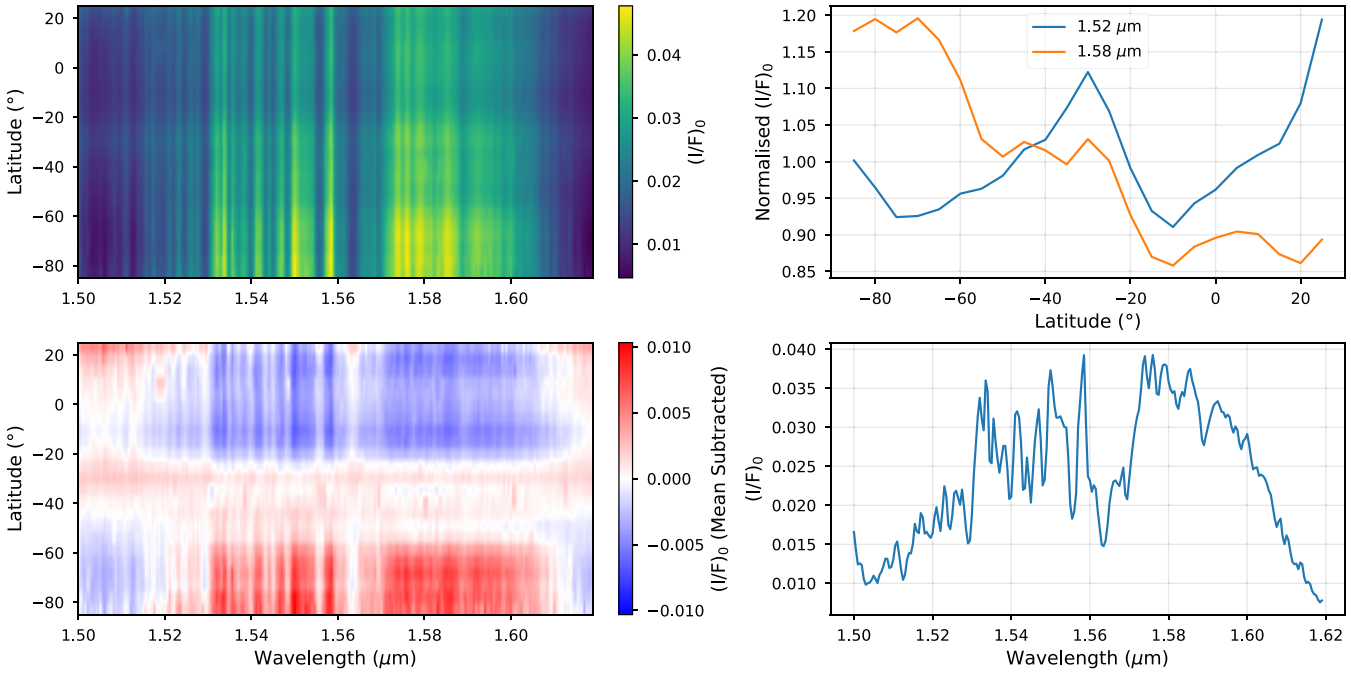

Figure 10. Top left: Minnaert-estimated nadir reflectivity as a function of latitude and wavelength. Bottom left: The same, with the mean over all latitudes subtracted. This shows that the southern latitudes are more reflective at most wavelengths. Top right: Reflectivity with latitude at a CH_4-absorbing wavelength (1.52 μm) and a wavelength of weak absorption (1.58 μm), showing markedly different trends. Bottom right: Nadir reflectivity averaged over all latitudes.

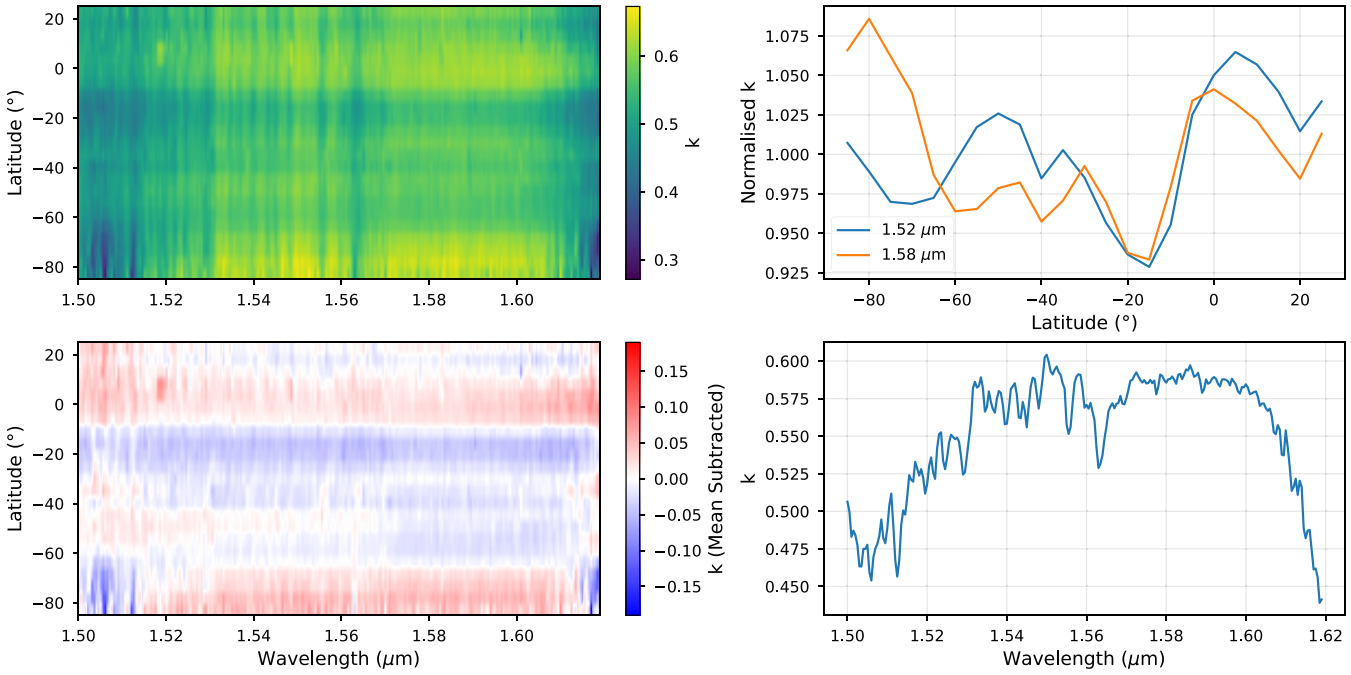

Figure 11. The same as Fig. 10, for the limb-darkening coefficient, k. Top left: k as a function of latitude and wavelength. Bottom left: k with the mean over all latitudes subtracted. The differences are small, but the mid-latitudes are more limb-brightened than the equator or pole. Top right: k with latitude at 1.52 μm and 1.58 μm, again showing somewhat different trends. Bottom right: k averaged over all latitudes.

small wavelength range. We also tried allowing the $n_{\rm imag}$ spectrum to vary for the deepest layer but found no improvement from this, so we kept it fixed to 10^{-4} for all wavelengths (corresponding to highly scattering particles). The $n_{\rm imag}$ spectra for the 2 bar layer and the extended haze layer were allowed to vary at four points (1.475, 1.525, 1.575, and 1.625 μm) with a correlation length of 0.1 μm to help smooth them. In our final set up, we had 15 varying parameters: 2 for the base cloud (opacity and fractional

Table 2. Aerosol size distribution parameters. The size distributions themselves are standard gamma distributions (J. E. Hansen 1971).

Aerosol layer	Mean radius (μm)	Radius variance
A1 (deep, extended)	0.1	0.05
A2 (discrete, ∼2 bar)	0.7	0.3
A3 (stratospheric haze)	0.05	0.05

scale height); 6 for the cloud at 2 bar (opacity, pressure, and 4 n_{imag} points); 6 for the extended haze (opacity, base pressure, and 4 n_{imag} points); and 1 scaling factor for our H_2S profile.

We experimented with many different changes to the aerosol parametrizations, including making the extended aerosol layer discrete, making the second aerosol layer extended, and adding a fourth aerosol layer similar to P. G. J. Irwin et al. (2022) to model upper tropospheric CH_4 clouds that potentially had not been masked out. However, these changes did not improve our goodness of fit so we did not use them.

3.2.3 *Nested sampling retrievals*

To fully understand the information that the data give us, we ideally would perform a retrieval at each latitude band using nested sampling. Nested sampling is a Bayesian Monte Carlo technique that iteratively samples the prior subject to increasing likelihood constraints, returning posterior samples and an estimate of the Bayesian evidence (J. Skilling 2006). Our forward model was using a multiple-scattering scheme to compute the radiance at two pairs of solar and zenith angles and ∼3000 wavelengths before convolving with the instrument function. While this should give a good level of accuracy, it was computationally expensive, and we found that allowing all 15 parameters to vary in a nested sampling retrieval for each latitude band would be prohibitively slow. In order to reduce the dimensionality, we first performed a Minnaert limb-darkening analysis over the whole disc for each of the observations to obtain disc-averaged spectra at viewing angles of 0.0°and 61.45°. We averaged these spectra across all observations to obtain a single pair of spectra for the entire planet. We then performed a nested sampling retrieval on these spectra using `archNEMESIS` (J. Alday et al. 2025). This retrieval was computationally intensive; it required roughly 2.5 million likelihood evaluations to converge, which took ∼10 thousand CPU hours on our computing system. The prior distributions were set to be Gaussians with standard deviations of 1 in log-parameter space, equivalent to what they would be in ordinary optimal estimation retrievals. However, we set the prior distribution of our H_2S scaling factor to be a wide log-uniform distribution between 10^{-5} (undetectable) and 10^2 (unreasonably large). We did this so that we would be able to determine how much our data set actually indicates the presence of H_2S without any prior bias. We ran nested sampling retrievals both with and without H_2S – the fitted spectra are shown in Fig. 12. Nested sampling gives us the Bayesian evidence for our models once they have converged. We can com-

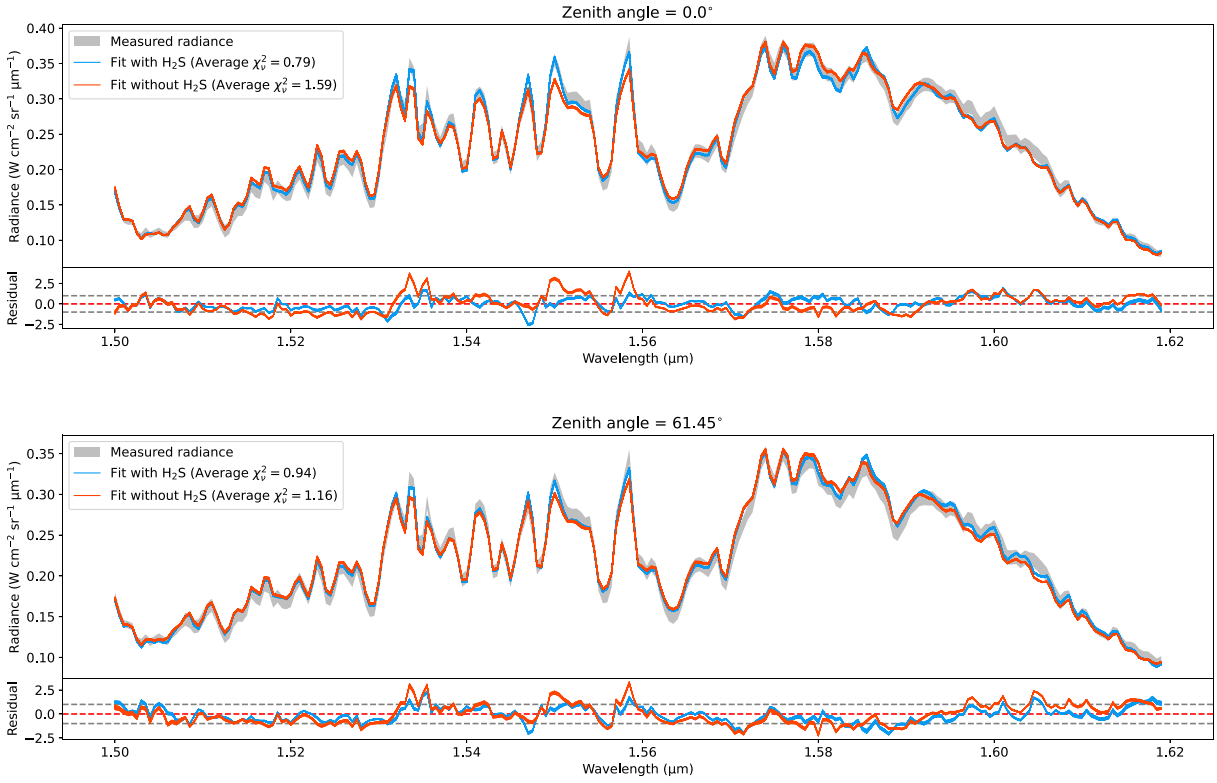

Figure 12. Envelopes of the best 1 per cent of models from our nested sampling disc analysis. The χ^2_ν values shown are averaged across these models as a diagnostic of the fit quality. The spectra at the zenith angle of 0.0° show a clear improvement when H_2S is included in the retrieval. The spectra at the zenith angle of 61.45° improve as well, but less so, due to the fact that the path length through the upper atmosphere is longer. This means that the light is more likely to be reflected or absorbed before reaching a pressure level with an appreciable amount of H_2S, and thus the H_2S signature is more subtle. As discussed in Section 3.2.1, the error on each spectrum is fixed to 2 per cent of the peak radiance.

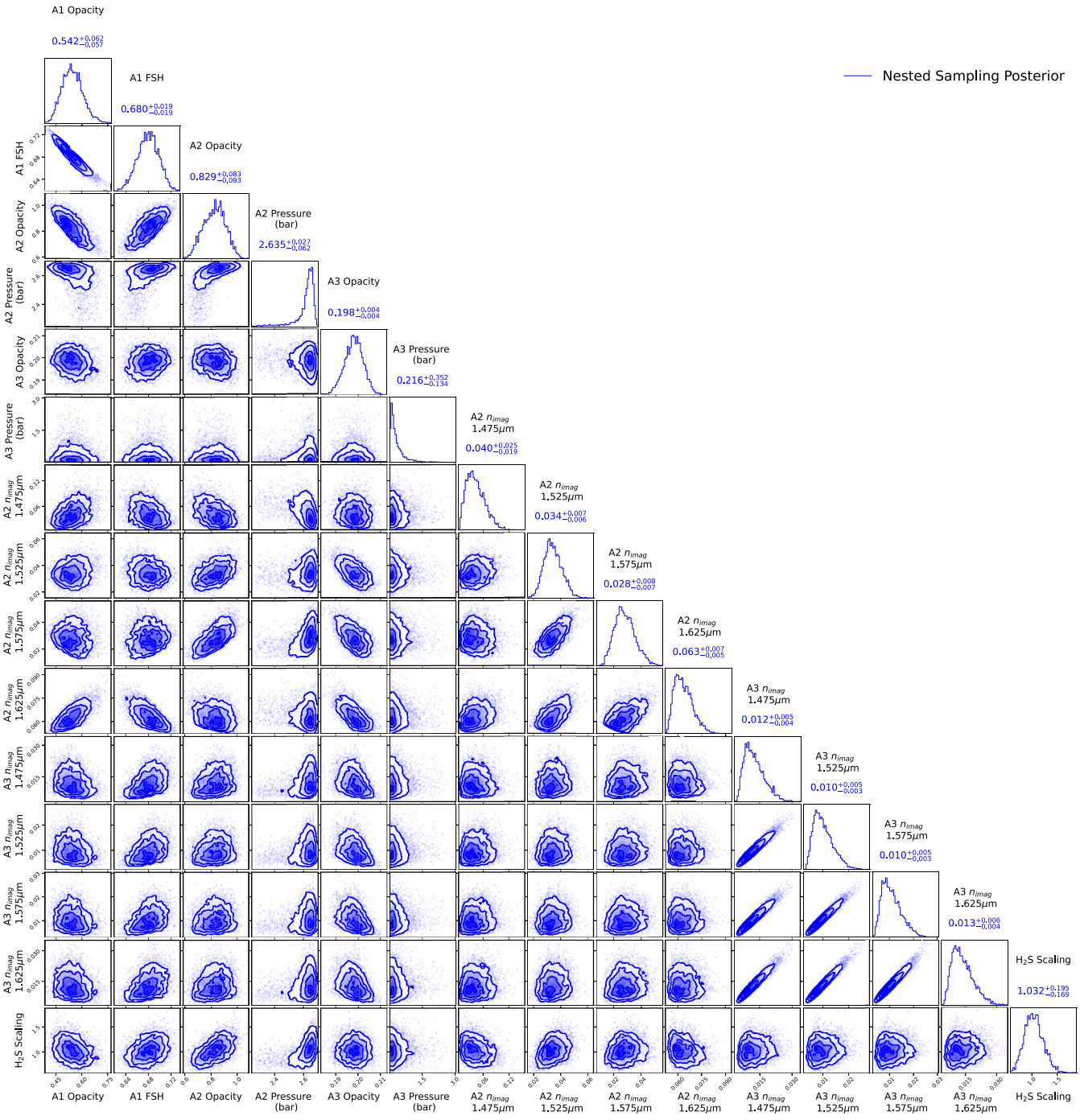

Figure 13. Corner plot showing the posterior distribution for our retrieval over the whole planetary disc. A1 refers to the deep aerosol layer, A2 to the ∼2 bar layer, and A3 to the stratospheric haze.

pare our models by comparing their Bayesian evidences - the Bayes factor is $K = \exp(\log(Z_{H_2S}) - \log(Z_{No\ H_2S}))$, where $\log(Z)$ is the log-evidence calculated in nested sampling. The model with H_2S included is decisively favoured by the Bayesian evidence ($\log(K) \sim 120$). The best-fitting spectrum from this model also yields smaller residuals than the best-fitting spectrum from the model without H_2S, with χ^2_ν values of 0.87 and 1.38, respectively.

The corner plot for our retrieval using H_2S is shown in Fig. 13. This shows the marginal distribution of each pair of parameters in the retrieved posterior distribution. From these nested sampling results, we found significant degeneracy between the opacity and fractional scale height of the deep aerosol layer and the opacity and n_{imag} spectrum of the ∼2 bar aerosol layer – this makes sense, as the two layers overlap. This is the 'cross-talk' discussed in P. G. J. Irwin et al. (2023) that can sometimes cause instability in optimal estimation retrievals. Also, the correlation between the opacity and fractional scale height of the deep aerosol layer was strong ($r \approx -0.95$) so we potentially could have

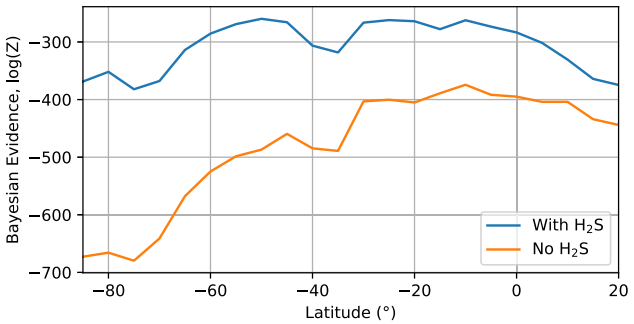

Figure 14. Comparison of log(Z) values with latitude for our retrievals with and without H_2S included. Clearly the presence of H_2S is strongly favoured, especially towards the pole where the spectral signature is strongest. Our uncertainty on log(Z) is roughly 0.5 at all latitudes.

combined them into a single parameter to reduce our parameter count by 1. However, we expected that there might be latitude bands with better sensitivity to this layer, where the degeneracy could be broken, so we kept these parameters separate. This turned out to be correct – close to the pole, these parameters became much less degenerate. Another interesting degeneracy in our results is between the values of the n_{mag} spectra of the stratospheric haze. These are all highly correlated with each other. It appears that we are able to strongly constrain the shape of this n_{imag} spectrum, but not its magnitude; i.e., we can tightly constrain the ratio of any two n_{imag} values but not the values themselves.

For our nested sampling retrievals on each latitude band, we fixed the two n_{imag} spectra to the retrieved n_{imag} spectra from the disc-averaged analysis, but we still allowed them to vary with a single multiplicative scaling factor on each of them – a 'darkening' parameter. In the disc-averaged retrieval, we found that the posterior distribution for the base pressure of the extended aerosol layer was poorly constrained, but with a median value of ∼0.2 bar. We fixed this parameter to this value. These changes brought our number of parameters down from 15 to 8. We found that this reduction was enough for our retrievals on latitude bands to run in a reasonable amount of time while still allowing the model to reproduce the data adequately. These retrievals typically took 100-200 thousand likelihood evaluations to converge (roughly 600 CPU hours on average).

In a similar way to our band-depth analysis, we tried running our latitude band retrievals only on the region of the spectrum containing the H_2S signature (1.58–1.60 μm) for the sake of computation speed. However, retrievals on this small region of the spectrum alone are insufficient to constrain the cloud structure at lower pressures, and thus result in less constraint on the H_2S abundance. The median H_2S scaling factor with latitude showed an increase at the southern mid-latitudes, but our uncertainties were high enough that we were unable to confidently conclude anything. In fact, retrieved results on this small region of the spectrum are consistent with both a decrease in H_2S abundance from the pole to the equator or from the equator to the pole (within a 95 per cent confidence interval). Unlike our simple band-depth model, which assumed a single reflecting aerosol layer, our more realistic aerosol model has many more degrees of freedom, and this narrow wavelength range does not provide sufficient constraint to break the degeneracies between the multiple aerosol parameters and the H_2S scaling factor. To remedy this, we widened our wavelength range to 1.50–1.62 μm. This worsened our average goodness of fit, but gave us sensitivity to a greater range of pressures (Fig. 4), so we were able to more tightly constrain all our parameters, including the H_2S abundance scaling factor.

We achieved a χ^2_ν value of less than 1.5 across the entire latitude range, with smaller residuals closer to the centre of our field of view (∼ 30° S). This is likely because latitude bands closer to this central point have more pixels and a larger zenith angle coverage, so we are able to determine the Minnaert parameters more accurately.

3.2.4 *Further testing*

We also performed retrievals on each latitude band without H_2S in our model. We find very large Bayes factors (log(K) > 50 for all latitudes) between the models with and without H_2S, which gives strong evidence for the presence of H_2S above the deep cloud (Fig. 14).

We also tested whether the presence of NH_3 would affect our retrievals. The presence of both H_2S and NH_3 above the NH_4SH cloud at ∼40 bar would be surprising – any detectable NH_3 signature would cast doubt on our modelling. Similar to P. G. Irwin et al. (2019), we find no evidence of NH_3. To make a detectable difference to the spectra, we need an extremely high supersaturation factor (∼1000), and even with this the presence of NH_3 increases the magnitude of the residuals rather than decreasing them.

In our retrievals, we have (fairly arbitrarily) set the relative humidity of CH_4 above the condensation level to be 50 per cent. Because we know that the retrieved H_2S scaling factor is very degenerate with the amount of CH_4, we might expect that not accounting for any CH_4 humidity variations could result in a misinterpretation of the data. However, in the wavelength regions where the H_2S signature is detectable, we are sounding quite deep in the atmosphere (∼3–5 bar). This means that the majority of the CH_4 absorption we see at these wavelengths is from below the condensation level where the abundance is highest. The result of this is that our retrieved H_2S abundance is strongly degenerate with the deep CH_4 abundance but is fairly independent of CH_4 variations higher up. This is confirmed by the results of retrievals with the CH_4 relative humidity set at 10 per cent and 100 per cent, which have a difference of less than 1 per cent in the retrieved H_2S scaling factor.

4 RESULTS AND DISCUSSION

An example corner plot (for the 30°S–20°S latitude band) is shown in Fig. 15. The results of our retrievals on each latitude band are shown in Fig. 16. The H_2S scaling factor shows a clear increase away from the south pole. There is a small local maximum at around 50°S (coinciding with a region where the zonal wind speed is zero (S. S. Limaye & L. A. Sromovsky 1991)), with the main maximum at 20°S. The H_2S abundance then decreases at 10°S before increasing again up to the equator. Moving northwards from the equator, the scaling factor decreases again. The results north of 10°N are quite dissimilar to the rest (e.g. the ∼2 bar aerosol darkening parameter is much higher). This is a region with quite poor zenith angle coverage and several discrete clouds, which may not have been perfectly masked out.

Similarly to our earlier band-depth analysis, we find that the deep H_2S ice cloud top is much deeper at the pole than at the

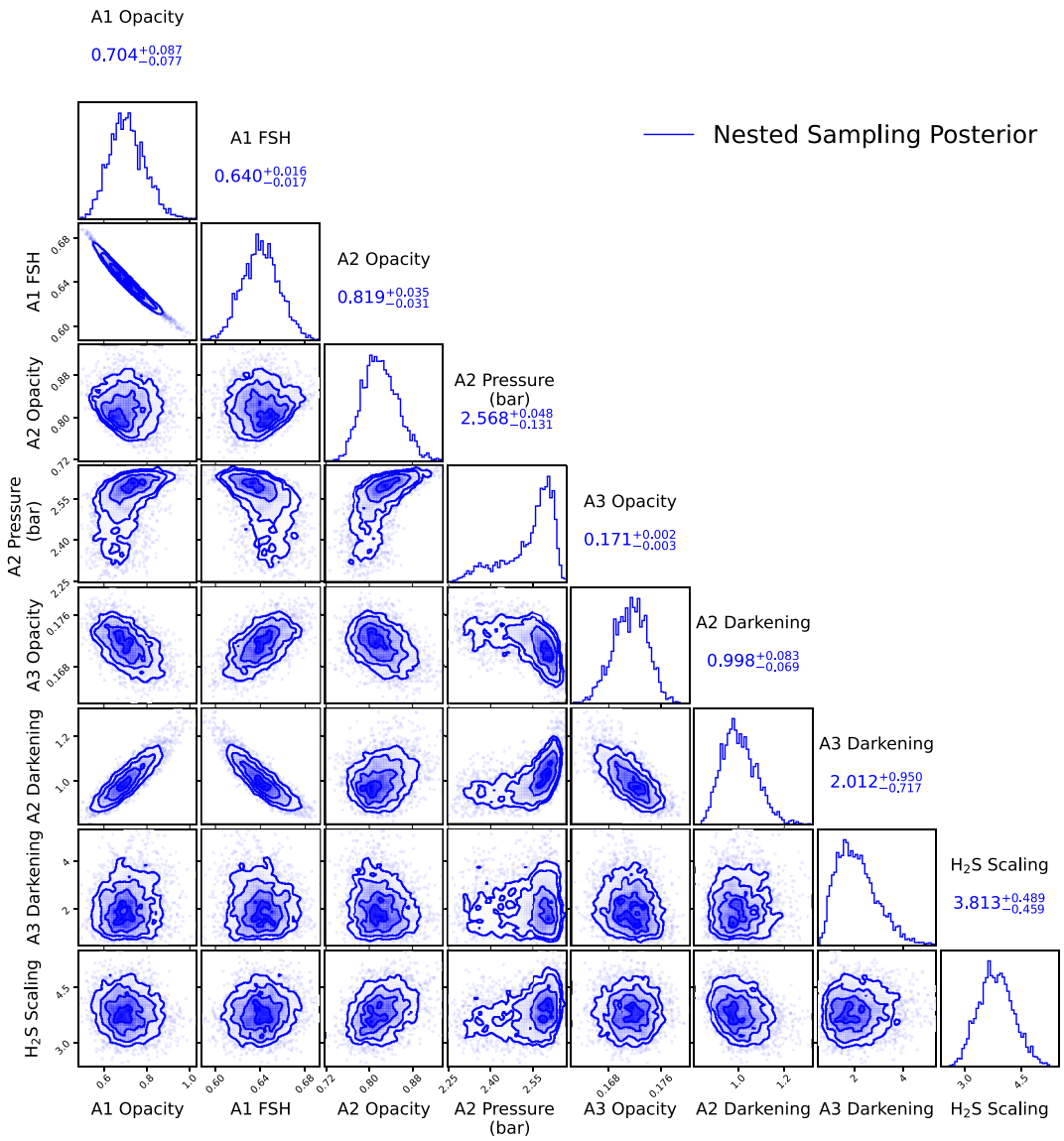

Figure 15. Example corner plot for one of our nested sampling retrievals with our reduced set of parameters, at 25°S. Again, A1 refers to the deep aerosol layer, A2 to the ∼2 bar layer, and A3 to the stratospheric haze. There is clear degeneracy between some of the parameters. For instance, the opacity and fractional scale height of the deep aerosol layer are anticorrelated. This makes sense – an increase of opacity will push the cloud top higher, so this must be accompanied by a decrease in scale height in order to have the correct cloud-top pressure and thus keep the spectrum looking roughly the same.

equator. A deeper cloud top means an increased column abundance of H_2S above the cloud – this gives us a stronger H_2S signature at polar regions, as shown in P. G. Irwin et al. (2019), despite a lower H_2S VMR there. The detectability of the polar H_2S signature is also increased by the fact that there is a lower CH_4 abundance and thus less CH_4 opacity. Fig. 17 shows our horizontal/vertical H_2S profile and the variation of cloud top height. We note that the results from this more physically accurate analysis seem less extreme than what was derived using the band-depth method. Our cloud-top pressures range from ∼3–4 bar instead of ∼2–4, and our maximum H_2S scaling factor south of the equator is ∼ 4 instead of ∼ 8. However, the general shape of the H_2S scaling factor profile with latitude is similar to the band-depth result, showing that this simplified analysis is still of value.

The deeper cloud top and decreased deep H_2S abundance at the pole could be explained by downwelling here, consistent with observations of the warm polar vortex in the mid-infrared (L. N. Fletcher et al. 2014; M. T. Roman et al. 2022). Similar to CH_4, H_2S-rich gas that upwells near the equator would move polewards and dry out, before descending at the pole – resulting in a lower abundance. The fact that the gas is depleted of H_2S means that the cloud will have a lower opacity above the condensation level, so the cloud top will be deeper (assuming the condensation level is not significantly higher due to warmer temperatures). The aerosols will also be transported downwards at a faster rate than those at equatorial latitudes due to the descending air.

We also performed retrievals with the CH_4 abundance prescribed to the latitudinal variation that was the best fit to the microwave observations in J. Tollefson et al. (2019). This latitudinal profile includes much less CH_4 than the results of P. G. J. Irwin et al. (2023), with a VMR of only 0.0055 at the pole (compared to ∼0.03 in the previous analysis). However, our model is still

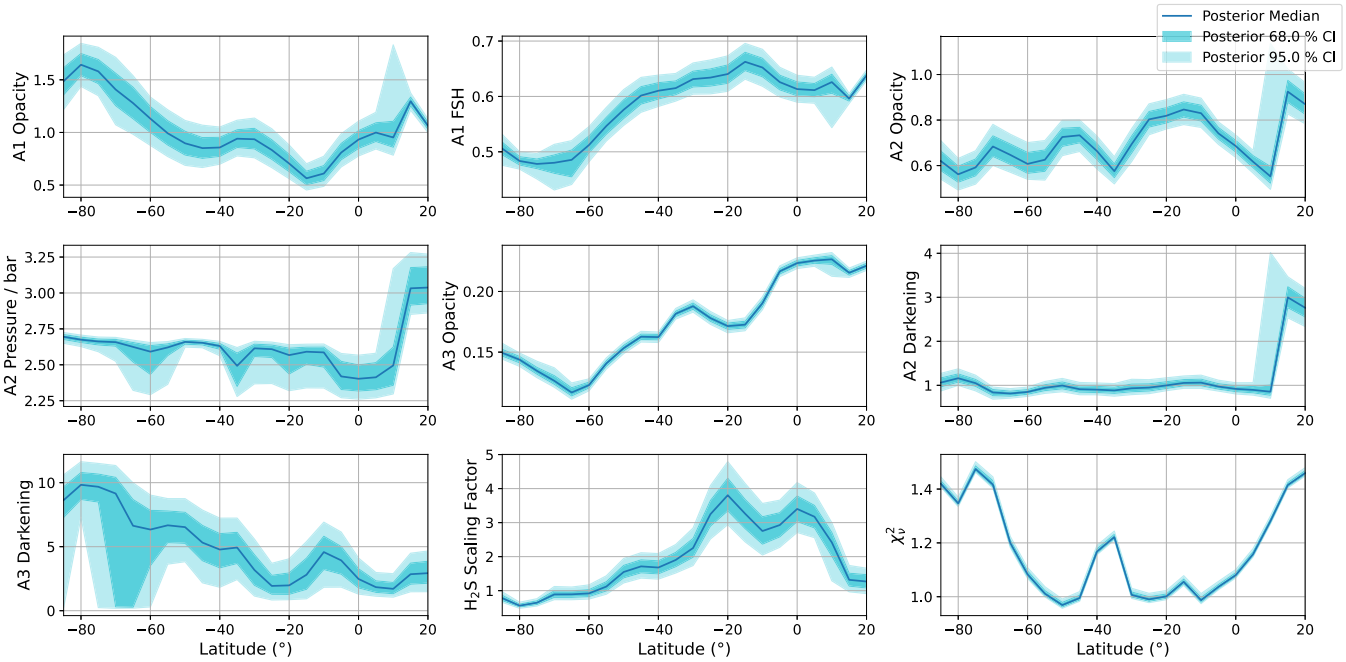

Figure 16. Retrieved variation of our 8 parameters with latitude, along with the χ^2_ν values of the posterior samples, to demonstrate the magnitude of the residuals as a diagnostic of the fit quality. There is a clear increase in H_2S abundance from the south pole towards the mid-latitudes and a local peak at the equator. 1-sigma (i.e. 68 per cent) and 2-sigma (95 per cent) confidence intervals are also plotted.

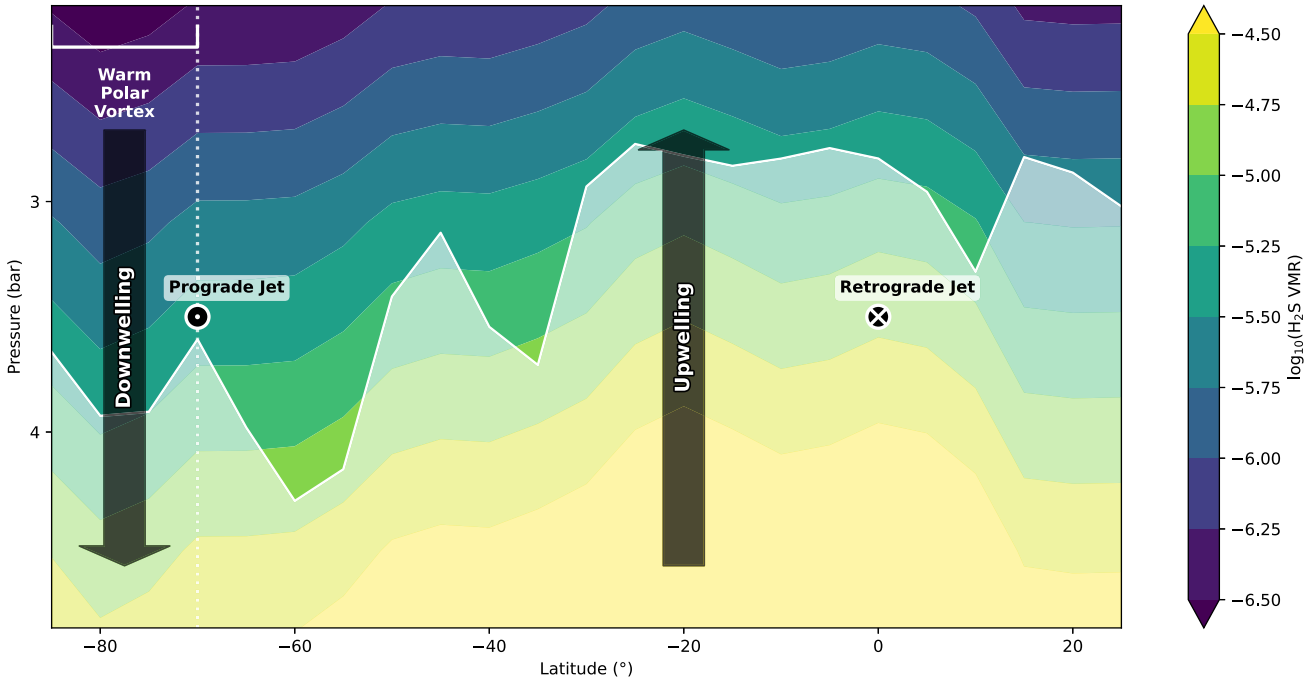

Figure 17. Diagram showing the H_2S VMR at varying pressures and latitudes. The white contour shows where the total aerosol opacity integrated downwards from the top of the atmosphere is equal to 1 (i.e. a measure of the cloud top). At every pressure level, there is more H_2S near the equator than near the pole as there is a higher deep abundance. However, the cloud top is deeper at the pole, so light from the Sun incident on the pole passes through more H_2S before being reflected back into space, giving a stronger spectral signature here.
The warm polar vortex is shown, as are the locations of the prograde and retrograde zonal jets, along with the locations of potential upwelling and downwelling.

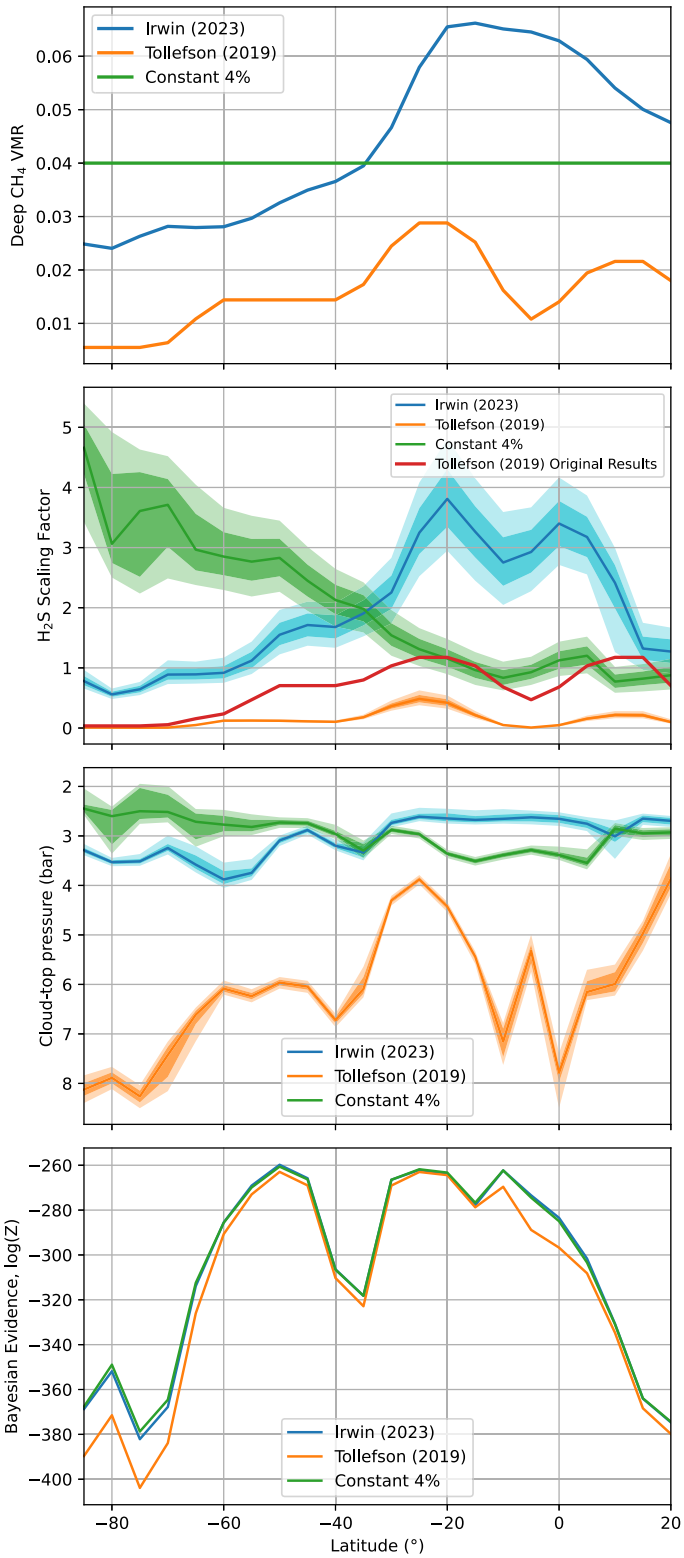

Figure 18. Retrieved variation of our H_2S profile scaling factor (second panel), cloud-top pressure (third panel), and Bayesian evidence (fourth panel) with latitude when using different latitudinal CH_4 profiles (first panel).

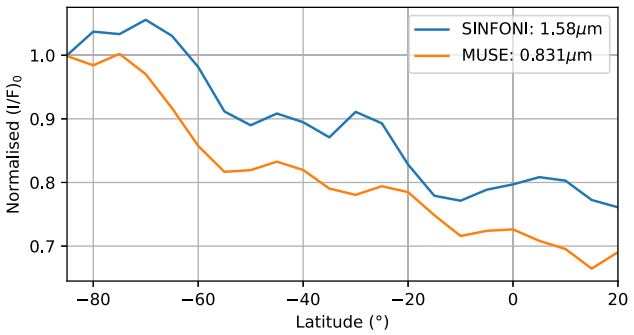

Figure 19. Reflectivity variation with latitude at 831nm from VLT/MUSE compared to our data at 1.58 μm where we are sounding deep in the atmosphere. There is clearly the same general trend, and the local peaks appear to mostly line up.

able to achieve good fits. We find a somewhat similar variation of H_2S between the south pole and 20°S as with the CH_4 profile from P. G. J. Irwin et al. (2023) (Fig. 18). However, we find a much stronger depletion north of this. Also, the magnitude of the H_2S scaling factor is much lower. This is because the CH_4 abundance is lower and, as discussed previously, there is a strong degeneracy between the two parameters in this wavelength range.

Additionally, we ran retrievals with the deep CH_4 VMR fixed to 0.04 at all latitudes. With this CH_4 profile, we find a significantly different H_2S variation with latitude, which decreases from the pole towards the equator. This is a reflection of the column abundance of H_2S above the cloud, and is more similar to the original variation suggested by P. G. Irwin et al. (2019).

Fig. 18 shows the H_2S variation for our different prescribed CH_4 latitudinal profiles. Clearly, it is not possible for us to determine the true abundance of H_2S without being certain of the true abundance of CH_4. The rough shape of the CH_4 latitudinal profile is generally agreed upon, with an increase from the pole to the equator, so we can be confident in saying that the H_2S profile follows a similar pattern, except with a probable decrease south of the equator.

The original H_2S variation found by J. Tollefson et al. (2019) is shown in red in Fig. 18, in the second panel. Clearly there is a difference between the magnitude of these previous results and our retrieved results when using their CH_4 abundances (orange). This is not unexpected, as we are sounding much higher in the atmosphere than this previous microwave analysis. There are also modelling differences; we have assumed a constant temperature profile with latitude, whereas temperatures are fit to the microwave observations. Despite their differences, the two profiles do show a very similar shape, with peaks at 25°S and 10°N. This reinforces the argument for upwelling near 20°S and shows agreement between analyses of Neptune's H_2S distribution in the microwave and near infrared. J. Tollefson et al. (2019) also experimented with some different vertical profiles of H_2S, but we are not sensitive enough to do this.

In addition to being degenerate with the CH_4 abundance, the magnitude of our retrieved H_2S abundance profile is also likely to be dependent on the assumed aerosol parametrization. There will be many alternative aerosol parametrizations that could fit our data (e.g. a continuous profile of a single species of aerosol as in P. G. Irwin et al. 2019), and these could affect the retrieved H_2S scaling factor by altering the weighting functions. However, the general retrieved shape of the H_2S profile is primarily driven by the relative variations in strength of the spectral signatures of CH_4 and H_2S, which suggests that our qualitative result of increased H_2S towards the mid-latitudes is likely to be relatively insensitive to the choice of aerosol parametrization, even though the magnitude of the retrieved scaling factor may be affected.

We can also compare the Bayesian evidence between the different latitudinal CH_4 profiles we tried (Fig. 18). There are some significant differences, especially towards the pole, where the CH_4 VMR from J. Tollefson et al. (2019) is very low. At the pole, the Bayes factor between the models using the P. G. J. Irwin et al. (2023) and J. Tollefson et al. (2019) profiles reaches $\log(K) \sim 20$, which is significantly in favour of the P. G. J. Irwin et al. (2023) value. One possibility is that our data can actually give a constraint on the CH_4 distribution. However, our base n_{imag} spectra were derived by setting the deep CH_4 VMR to 4 per cent, which is significantly greater than the polar J. Tollefson et al. (2019) value of 0.55 per cent. It is likely that there may be some degeneracy between the shape of the n_{imag} spectra and the CH_4 abundance, and so prescribing both of these enforces a limit on how well our model can represent the data. To completely understand this, a more thorough analysis would involve allowing the n_{imag} spectra and the deep CH_4 VMR to freely vary during our latitudinal retrievals, but this is beyond both our computational limits and the scope of this work.

P. G. J. Irwin et al. (2023) found an interesting variation of reflectivity with latitude near 831 nm (where the CH_4 absorption is very weak) with bright zones separated by ∼25°. These bright zones were attributed to a brightening of the aerosol particles in the deep aerosol layer at wavelengths greater than 650 nm.

We find a somewhat similar variation in reflectivity with latitude in our observations at wavelengths of weak CH_4 absorption (Fig. 19). However, we are not allowing the imaginary refractive index of the deep aerosol particles to vary, so how is our model accounting for this variation? Several of our parameters (aerosol-2 opacity, aerosol-3 darkening, and perhaps the H_2S scaling factor) have local increases or decreases near the peaks of reflectivity; it seems as though our model is fitting to this variation in quite a complex way. Most of the parameters are degenerate with the prescribed CH_4 abundance, and we are only fitting over a small wavelength range, so there may not be enough constraint to determine a single cause of the near-infrared reflectivity variation.

To fully understand this, future observations which can constrain both the CH_4 and H_2S abundances simultaneously are needed. Our modelling has shown that at higher spectral resolutions it is possible to independently extract CH_4 and H_2S variations, so these observations would require an instrument that can achieve high signal-to-noise at a higher spectral resolution than SINFONI – for example, the James Webb Space Telescope's NIRSpec instrument with the G140H/F100LP grating/filter combination.

Although we used nested sampling for the majority of our analysis, we did perform identical comparative optimal estimation runs. We found that the two methods yielded mostly similar results in both the retrieved parameter values and the posterior uncertainties. We have many more wavelengths than varying parameters, and our parameters are not particularly degenerate, which makes it easier for gradient-based methods like optimal estimation to converge to the optimum. However, for parameters that are poorly constrained or have non-Gaussian posterior distributions we find that the two methods do give different results. For

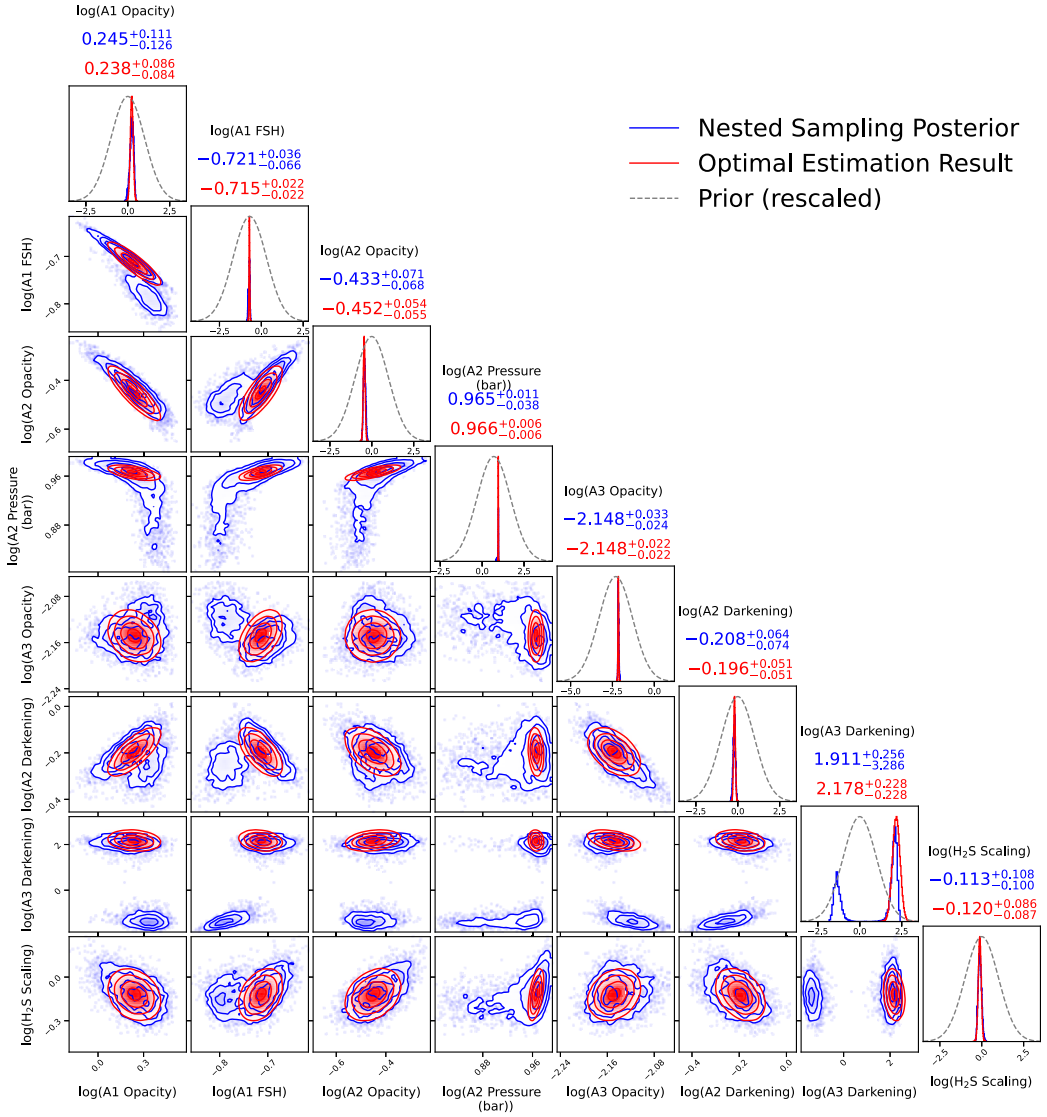

Figure 20. Comparison of nested sampling and optimal estimation results for the 70°S–60°S latitude band. Note that the parameters are in log-space. Gaussian posteriors are assumed for the optimal estimation results. Prior distributions are shown by the dashed grey line in the 1D plots, and have been scaled for clarity. The 1D plots are on a different scale to the 2D plots so that the width of the prior can be seen. For the purposes of this comparison, we used a log-Gaussian for the nested sampling H_2S scaling factor prior distribution rather than a uniform distribution, to ensure the methods had identical starting conditions (as our optimal estimation code always assumes Gaussian priors). Clearly optimal estimation has converged to one of the two possible modes found by nested sampling. This leads to an underestimation of the uncertainty, although we note that the uncertainty on the H_2S scaling factor is similar between the two methods, as it is similar across the two modes and has quite a Gaussian posterior distribution.

example, near the pole, we have less constraint on the darkening parameter for the extended haze layer. In fact, we find that this parameter is bimodal in some latitude bands. For the band centred at 65°S (Fig. 20) the darkening parameter can either be ∼10, corresponding to n_{imag} values of ∼0.1, or ∼0.2, which corresponds to n_{imag} values of ∼0.002. Most of the other parameters are not strongly affected by this bimodality (in particular, it is reassuring to see that the H_2S scaling factor has a very similar distribution for both modes) except for the fractional scale height of the deep aerosol layer. The spectra for this latitude band are consistent either with dark haze particles and a more vertically extended deep aerosol layer, or with scattering haze particles and a less vertically extended deep aerosol layer. Of course, optimal estimation cannot show this bimodality and converges to one of the modes. By adjusting the initial parameter values, it is possible for optimal estimation to converge to the other mode. Fig. 20 also shows that optimal estimation underestimates the posterior error on the pressure of the discrete aerosol layer, as its posterior distribution from nested sampling has a long tail. Clearly, in some cases, optimal estimation can give poor estimates of parameter error. This is informative for future work – optimal estimation can provide rapid parameter determination and is well-suited to exploratory analyses when the posterior is well-behaved, but nested sampling should be preferred for both robust uncertainty estimation (particularly when the posteriors are asymmetric or multimodal) and for comparing different model parametrizations via the Bayesian evidence.

5 CONCLUSIONS

We have used near-infrared observations from VLT/SINFONI in 2018 to search for H_2S in Neptune's atmosphere. We use a limb-darkening approximation to average our observations into latitude bands, and we use nested sampling to fit a parametrized aerosol model (along with our H_2S VMR scaling factor) to spectra reconstructed at two zenith angles for each latitude band. We also prescribe a CH_4 variation with latitude from previous work (P. G. J. Irwin et al. 2023). The presence of H_2S significantly improves our fits at all latitudes (Fig. 14) and we are able to show its spectral signature (Fig. 8). We are also able to show that its abundance varies with latitude.

We can only constrain the H_2S variation with latitude if we can constrain the CH_4 variation. The general shape of the CH_4 variation is accepted, so we are able to constrain the general shape of the H_2S variation; however, we are unable to confidently constrain the details of the shape or the magnitude of the H_2S abundance. Assuming a CH_4 abundance that increases from the pole to the equator, the shape of the latitudinal variation of H_2S with latitude is similar to that found in J. Tollefson et al. (2019), increasing in abundance from the south pole to $\sim$20°S. North of this the abundance of H_2S decreases and then has a second peak between the equator and 20°N. Earlier analysis of *H*-band Gemini/NIFS observations (P. G. Irwin et al. 2019), which did not prescribe a latitudinally variable CH_4 abundance, found a stronger signature of H_2S near the south pole which was interpreted as being caused by higher H_2S abundance there. This new analysis of the same wavelength region with VLT/SINFONI observations finds the same variation in the strength of the H_2S signature. However, a latitudinally variable CH_4 abundance is included in this new analysis, and we find that the increased H_2S signature near the pole is more consistent with a lower H_2S abundance and a deeper cloud-top pressure of the H_2S/haze cloud. Our retrieved H_2S latitudinal abundance is more consistent with the variation concluded from microwave observations (J. Tollefson et al. 2019), which thus accounts for the previous discrepancy between near-infrared and microwave determinations of the H_2S latitudinal abundance. The latitudinal variation of the pressure of the top of the deep H_2S ice cloud, combined with the H_2S variation, is consistent with downwelling at the pole and upwelling at $\sim$20°S – suggesting, in agreement with J. Tollefson et al. (2019), that this circulation pattern extends from the CH_4 condensation level to $>\sim$5 bar.

ACKNOWLEDGEMENTS

We are grateful to the United Kingdom Science and Technology Facilities Council (STFC) for funding this research. STFC Doctoral Training Partnership grant reference: ST/Y509474/1. The observations were performed at the European Southern Observatory (ESO), Proposal 0101.C-0081. Patrick Irwin and Jack Dobinson were supported by a Leverhulme Trust Research Project Grant (reference RPG-2023-028). Nicholas Teanby was supported by STFC Grant reference ST/Y000676/1. Leigh Fletcher was supported by STFC Grant reference UKRI1205. For the purpose of open access, the author has applied a Creative Commons Attribution (CC BY) licence to the Author Accepted Manuscript version arising from this submission.

DATA AVAILABILITY

The raw VLT/SINFONI data sets used in this work are available from the ESO Portal at https://archive.eso.org/eso/eso_archive_main.html. Retrievals were performed using archNEMESIS, which is available at https://github.com/juanaldayparejo/archnemesis-dist.

REFERENCES

Alday J., Penn J., Irwin P., Mason J., Yang J., Dobinson J., 2025, J. Open Res. Softw. 13, 10
Atreya S. K., Wong A.-S., 2005, Space Sci. Rev., 116, 121
Borysow A., Frommhold L., 1989, ApJ, 341, 549
Campargue A., Leshchishina O., Wang L., Mondelain D., Kassi S., 2013, J. Mol. Spect., 291, 16
Eisenhauer F. et al., 2003, in Iye M., Moorwood A. F. M., eds, Proc. SPIE Conf. Ser. Vol. 4841, Instrument Design and Performance for Optical/Infrared Ground-based Telescopes. SPIE, Bellingham, p. 1548
Fletcher L. N., de Pater I., Orton G. S., Hammel H. B., Sitko M. L., Irwin P. G., 2014, Icarus, 231, 146
Fletcher L. N., de Pater I., Orton G. S., Hofstadter M. D., Irwin P. G. J., Roman M. T., Toledo D., 2020, Space Sci. Rev., 216, 21
Gordon I. et al., 2022, J. Quant. Spect. Rad. Trans., 277, 107949
Hansen J. E., 1971, J. Atmos. Sci., 28, 1400,
Hartmann J.-M., Boulet C., Brodbeck C., van Thanh N., Fouchet T., Drossart P., 2002, J. Quant. Spect. Rad. Trans., 72, 117
Irwin P. et al., 2014, Icarus, 227, 37
Irwin P. G. J., Toledo D., Garland R., Teanby N. A., Fletcher L. N., Orton G. S., Bézard B., 2019, Icarus, 321, 550
Irwin P. G. J. et al., 2022, J. Geophys. Res.: Planets, 127, e2022JE007189
Irwin P. G. J. et al., 2023, J. Geophys. Res.: Planets, 128, e2023JE007980
Irwin P. G. J., Hill S. M., Fletcher L. N., Alexander C., Rogers J. H., 2025, J. Geophys. Res.: Planets, 130, e2024JE008622
James A. et al., 2023, J. Geophys. Res.: Planets, 128, e2023JE007904
Karkoschka E., Tomasko M. G., 2011, Icarus, 211, 780
Lacis A. A., Oinas V., 1991, J. Geophys. Res.: Atmospheres, 96, 9027
Lellouch E. et al., 2010, A&A, 518, L152
Limaye S. S., Sromovsky L. A., 1991, J. Geophys. Res.: Space Physics, 96, 18941
Lindal G. F., 1992, AJ, 103, 967
Meftah M., Sarkissian A., Keckhut P., Hauchecorne A., 2023, Remote Sens., 15, 3560
Minnaert M., 1941, ApJ, 93, 403
Roman M. T. et al., 2022, Planet. Sci. J., 3, 78
Skilling J., 2006, Bayesian Anal., 1, 833
Tollefson J., de Pater I., Luszcz-Cook S., DeBoer D., 2019, AJ, 157, 251

This paper has been typeset from a TEX/LATEX file prepared by the author.